



## RESEARCH LETTER

10.1002/2015GL066559

## Key Points:

- Self-organizing maps are used for a joint interpretation of tomography models
- Deep prebasin sediments were revealed below asymmetric basin structure
- Seismicity distribution reflects geometry of derived lithological units

## Correspondence to:

B. Braeuer,  
ben@gfz-potsdam.de

## Citation:

Braeuer, B., and K. Bauer (2015), A new interpretation of seismic tomography in the southern Dead Sea basin using neural network clustering techniques, *Geophys. Res. Lett.*, 42, 9772–9780, doi:10.1002/2015GL066559.

Received 13 OCT 2015

Accepted 5 NOV 2015

Accepted article online 9 NOV 2015

Published online 27 NOV 2015

# A new interpretation of seismic tomography in the southern Dead Sea basin using neural network clustering techniques

Benjamin Braeuer<sup>1</sup> and Klaus Bauer<sup>1</sup>
<sup>1</sup>GFZ German Research Centre for Geosciences, Potsdam, Germany

**Abstract** The Dead Sea is a prime location to study the structure and development of pull-apart basins. We analyzed tomographic models of  $V_p$ ,  $V_s$ , and  $V_p/V_s$  using self-organizing map clustering techniques. The method allows us to identify major lithologies by their petrophysical signatures. Remapping the clusters into the subsurface reveals the distribution of basin sediments, prebasin sedimentary rocks, and crystalline basement. The Dead Sea basin shows an asymmetric structure with thickness variation from 5 km in the west to 13 km in the east. Most importantly, we identified a distinct, well-defined body under the eastern part of the basin down to 18 km depth. Considering its geometry and petrophysical signature, this unit is interpreted as a buried counterpart of the shallow prebasin sediments encountered outside of the basin and not as crystalline basement. The seismicity distribution supports our results, where events are concentrated along boundaries of the basin and the deep prebasin sedimentary body. Our results suggest that the Dead Sea basin is about 4 km deeper than assumed from previous studies.

## 1. Introduction

The Dead Sea transform fault (DST), one of the largest transform faults in the world with a length of about 1000 km, is a part of the boundary between the Arabian and the African plates (Figure 1). The relative left-lateral motion of these two plates started in the early Miocene (~20 Ma), causing a total shift of about 107 km [e.g., Quennel, 1958; Freund et al., 1970]. In parallel to the transform motion, the formation of the Dead Sea basin (DSB) was initiated, resulting in one of the largest pull-apart basins of the world [Garfunkel, 1981; Garfunkel and Ben-Avraham, 1996]. The total length of the basin is 107 km, i.e., consistent with the shift along the DST [Quennel, 1958], while it is only 15–17 km wide. The structural setting of the basin and its development as a pull-apart is mainly controlled by two laterally stepping master strike-slip faults [Garfunkel, 1997]. These master faults mark the western and eastern boundary of the DSB. The western boundary is built up by several faults: the western strike-slip fault (WSF), the continuation of the Jericho fault, and various normal faults where the western boundary fault (WBF) is the most important one [Garfunkel, 1997; Sagi et al., 2003]. Many authors point out the asymmetry of the basin in the E-W direction with a deep and nearly vertical eastern boundary fault (EBF) and a shallower western boundary fault inclined to the east [e.g., Frieslander and Ben-Avraham, 1989; Garfunkel and Ben-Avraham, 1996; Garfunkel, 1997; Shamir, 2006; Hofstetter et al., 2012].

The basin is filled by thick layers of sediments. Clastics and evaporites were deposited during periods of different climate and varying water sources (fresh or salt), which transported the sediments into the basin [Zak, 1967]. In the southern DSB (SDSB) the upper 4 km of the basin fill consists of fluvial and lacustrine clastics, which were deposited during Pleistocene and Holocene. The Neogene evaporites ascended at fault zones and formed two prominent salt diapirs within the basin: The Sedom diapir in the southwest of the basin (below Mount Sedom in Figure 1) and the Lisan diapir (below Lisan peninsula in Figure 1), located in the center of the basin. Miocene sandstones and conglomerates, the first deposits after the beginning of the basin formation, are found below the Neogene sediments [Kashai and Croker, 1987; Gardosh et al., 1997]. The prebasin sediments form the lowest layer of the basin fill, as well as the uppermost 3–5 km thick layer east and west of the basin [Mechie et al., 2009]. The prebasin sediments consist of mesozoic carbonates from a former continental margin and sediments of Permian age [Gilboa et al., 1993]. While this near-surface structure was already described [e.g., Garfunkel, 1997], the deeper structure and its origin are still under debate. From a gravity study ten Brink et al. [1993] estimated about 5 km thickness of prebasin sediments and a maximum depth to the basement of 16 km. From a NS trending seismic refraction profile within the basin, a maximum prebasin sediment thickness of 6 km and 14 km

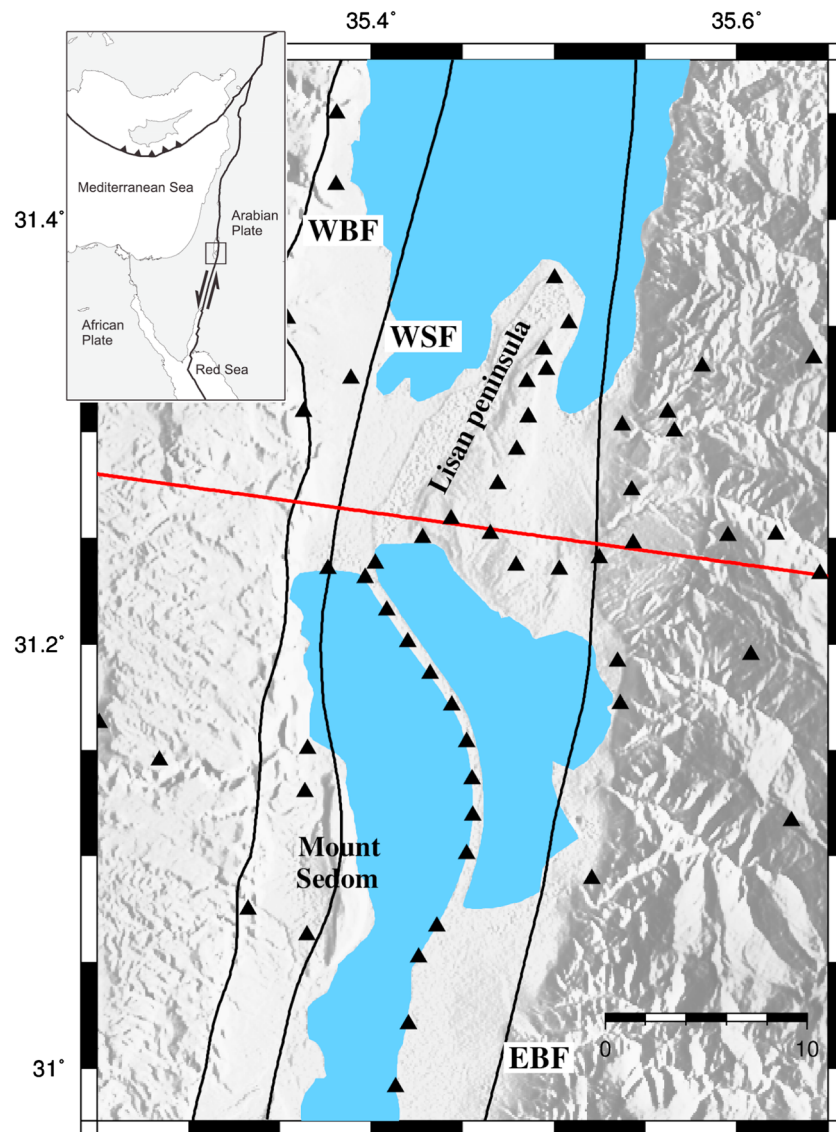


**Figure 1.** Topographic map of the study area. Seismological stations are shown as black triangles. Only the main faults are indicated as black lines. Eastern boundary fault (EBF); western strike-slip fault (WSF), and western Boundary fault (WBF). The red line is indicating the location of the 2-D profile.

depth to the basement was determined [Ginzburg and Ben-Avraham, 1997]. To explain this unusual great depth of a sedimentary basin, Ben-Avraham and Schubert [2006] developed the concept of the symmetric deep “drop down” southern Dead Sea basin. According to them, the southern DSB was formed during the first stage of the formation of the DSB when the tips of two propagating faults overlapped in this area. The fault tips curved toward each other, resulting in an isolated block of crust and lithosphere that dropped into the mantle.

ten Brink *et al.* [2006] identified a new midcrustal feature underneath the southern DSB which could represent a key structure for the understanding of the DSB development and other sedimentary basins in general [ten Brink and Flores, 2012]. Their  $P$  velocity model was derived from modeling and tomographic inversion of refraction seismic data and consists of basin and prebasin sediments down to about 10 km depth. In addition, an anomalous zone of relatively low  $V_p$  was found below the basin extending down to 18 km depth. The lower crust and Moho are undisturbed in this model. ten Brink *et al.* [2006] argued that softening mechanisms such as shear heating, grain-size sensitive flow, and reaction softening could be responsible for the low  $V_p$  values in the middle crust. More specifically, ten Brink and Flores [2012] suggested that the lower  $V_p$  values

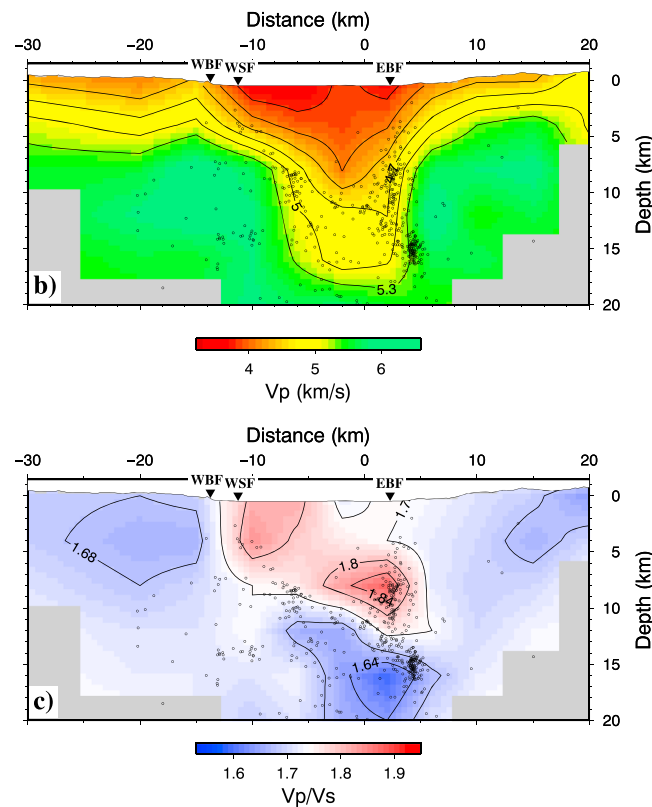


**Figure 2.** (a) Two-dimensional  $P$  velocity model from Braeuer *et al.* [2012b] with contour lines and black circles indicating the local earthquakes. (b) 2-D model of  $V_p/V_s$  ratios with contour lines and black circles indicating the local earthquakes. The surface traces of the faults (Figure 1) are indicated by black triangles.

by Bauer *et al.* [2008, 2012], to carry out a clustering of  $V_p$ ,  $V_s$ , and  $V_p/V_s$  to identify seismic velocity classes, which can be interpreted in terms of major lithologies. We will show that such a clustering can reveal the extent of basin, prebasin, and basement structures in the model, and a lithological interpretation can be provided based on the seismic signature of each cluster. The results provide a new perspective on the general architecture of the southern DSB.

## 2. Local Earthquake Tomography

The basic data for our study was generated through a temporary seismic network of 65 stations, operating 18 month in the southern Dead Sea basin which was presented in detail in Braeuer *et al.* [2012a] and Braeuer *et al.* [2012b]. The local earthquake tomography with 530 well constrained events ( $-0.5 \leq M_d \leq 4.5$ ) consisted of 13,970  $P$  and 12,760  $S$  wave arrival time observations, i.e., an average of 50 traveltime picks per event. The tomography revealed the 2-D and 3-D structure of  $P$  velocities and  $V_p/V_s$  ratios as well as the distribution of the local seismicity [Braeuer *et al.*, 2012b, 2014].

A simultaneous inversion of hypocentral parameters,  $V_p$ , and  $V_p/V_s$  ratios was performed, using the inversion code SIMULPS [Thurber, 1983; Thurber, 1993; Eberhart-Phillips, 1986; Evans *et al.*, 1994]. The method and results were described in detail in Braeuer *et al.* [2012b], and a very short summary will be given here. The results were verified by numerous synthetic tests, e.g., model recovery tests.

Due to the long-term parallel movement of the bordering strike-slip faults, the study area is dominated by a two-dimensional structure (Figure 1). This was also confirmed by the tomography study of Braeuer *et al.* [2012b], and thus, we will focus on the two-dimensional structure in this paper. The  $P$  velocity model revealed a strong negative anomaly in the area of the basin (Figure 2a). Down to a depth of 18 km the velocities do

are an indication for interconnected ductile shearing as consequence of alteration processes and presence of pore fluids, which ultimately caused the rapid subsidence and elongation of the DSB. ten Brink and Flores [2012] moreover propose that similar processes were responsible for the rapid, enigmatic subsidence of the North Sea basin at the onset of the North Atlantic mantle plume.

For our study it is worth to note that the suggestions of ten Brink *et al.* [2006] and ten Brink and Flores [2012] to explain the midcrustal lower  $P$  velocities are based on the crucial assumption that the discussed material is located below the prebasin sediments and forms part of the basement. However, additional petrophysical constraints from joint interpretation of  $V_p$  and  $V_p/V_s$  as presented in this paper suggest that this low  $V_p$  anomaly represents prebasin sediments instead. Tomographic models of  $V_p$  and  $V_p/V_s$  were derived for the southern Dead Sea basin from local earthquake tomography [Braeuer *et al.*, 2012b]. In the following we apply self-organizing maps (SOM), a neural network method introduced by Kohonen [2001] and modified

not exceed 5.3 km/s inside the basin while below the shoulders east and west of the basin already at 8 km depth velocities of about 6 km/s are found (Figure 2a). The model of the  $V_p/V_s$  ratios shows higher ratios ( $>1.73$ ) in the area of the basin and lower values ( $<1.73$ ) outside the basin (Figure 2b). These higher values for the  $V_p/V_s$  ratio are reaching depths of 7 km at the western boundary and about 12 km at the eastern boundary, respectively (Figure 2b). The 3-D models in Braeuer *et al.* [2012b] showed that the average values of 1.74 close to the surface in the eastern part of the basin. This is caused by the Lisan salt dome in this area below the Lisan peninsula (Figure 1) due to the low  $V_p/V_s$  ratio of salt compared to other sediments. Thus, Braeuer *et al.* [2012b] concluded that the sedimentary basin fill is clearly imaged through higher  $V_p/V_s$  ratios and low  $V_p$ . The basin shows an asymmetric structure with depth of 7 km at the western boundary (verified by a borehole study [Gardosh *et al.*, 1997]) and a depth of 12 km at the eastern boundary. This asymmetric structure of the basin fill is caused by the normal faulting at the western boundary, in agreement with the recent transtensional regime in the basin [Garfunkel, 1981; Smit *et al.*, 2010; Braeuer *et al.*, 2014]. However, the  $P$  wave velocity model shows low  $P$  wave ( $<5.5$  km/s) velocities and low  $V_p/V_s$  ratios down to 18 km depth. Braeuer *et al.* [2012b] could not find a reasonable explanation for the observed anomaly under the basin. Therefore, our study used the SOM clustering method to find more details about the deeper structure below the Dead Sea basin.

### 3. SOM Clustering Method

The combined interpretation of different seismic properties ( $V_p$ ,  $V_s$ , surface wave velocity,  $V_p/V_s$ , Poisson's ratio), instead of the separate treatment of each property, can be used to better constrain the lithological nature of seismic earth models [e.g., Holbrook *et al.*, 1992; Christensen, 1996; Bauer *et al.*, 2003]. A common approach is to crossplot seismic properties such as  $V_p$  against  $V_p/V_s$  in order to find clusters which are related with distinct rock types frequently occurring in the studied subsurface region [e.g., Bauer *et al.*, 2003; Paasche *et al.*, 2006]. The remapping of the found clusters into the subsurface model reveals the distribution of the rock types at depth. The interpretation can be based on the petrophysical signature of each cluster and comparison with rock properties reported in the literature and by linkage with surface geology or borehole information, if available [Bauer *et al.*, 2003].

An alternative approach which is suited for the combined interpretation of different geophysical models makes use of the SOM neural network [Kohonen, 2001]. The method can be used as substitute for the widely used statistical method called k-means clustering [Baço *et al.*, 2005]. Successful applications of SOM for the joint interpretation of different seismic tomography results were reported from a number of case studies [Tselentis *et al.*, 2007; Bauer *et al.*, 2008; Stankiewicz *et al.*, 2010; Ryberg *et al.*, 2012; Muksin *et al.*, 2013]. Here we apply the SOM method of Bauer *et al.* [2008, 2012] to combine the tomograms of  $V_p$ ,  $V_s$ , and  $V_p/V_s$  derived for the Dead Sea basin as shown in Figure 2.

The general concept of our SOM method is described by means of a test with synthetic models (Figure 3). For a given model geometry, seismic parameters were defined for each model body. Random variations in the seismic velocity parameters were added to simulate realistic conditions (Figure 3a). The images were generated to demonstrate the performance of the method and to illustrate the individual steps of the work flow. We are not considering the resolving power of the inversion methods at this point. The neural network consists of a number of input neurons forming the input layer and a two-dimensional arrangement of neurons, called Kohonen layer (Figure 3b). The work flow includes (1) preparation of input vectors, (2) unsupervised learning by input examples, (3) cluster identification, and (4) classification of all input vectors and derivation of a lithological model.

In step (1), the input vectors are formed for each grid node of the tomographic model. We combine the 2-D models of  $V_p$ ,  $V_s$ , and  $V_p/V_s$ . Such a parameter combination was also suggested by Tselentis *et al.* [2007]. The models are first interpolated onto a common grid. To avoid inaccuracies, we apply the identical linear B-spline interpolation as used within the tomography package [Thurber, 1983]. Each model block  $k$  is then associated with an input vector defined by

$$\vec{x}_k = \left( Vp_k, Vs_k, \frac{Vp_k}{Vs_k} \right)^T. \quad (1)$$

Step (2) represents the learning phase. Each neuron  $i$  at the Kohonen layer is associated with a weight vector  $\vec{m}_i$  of the same dimension as the input vectors. At the first iteration, the components of the weight vectors are set

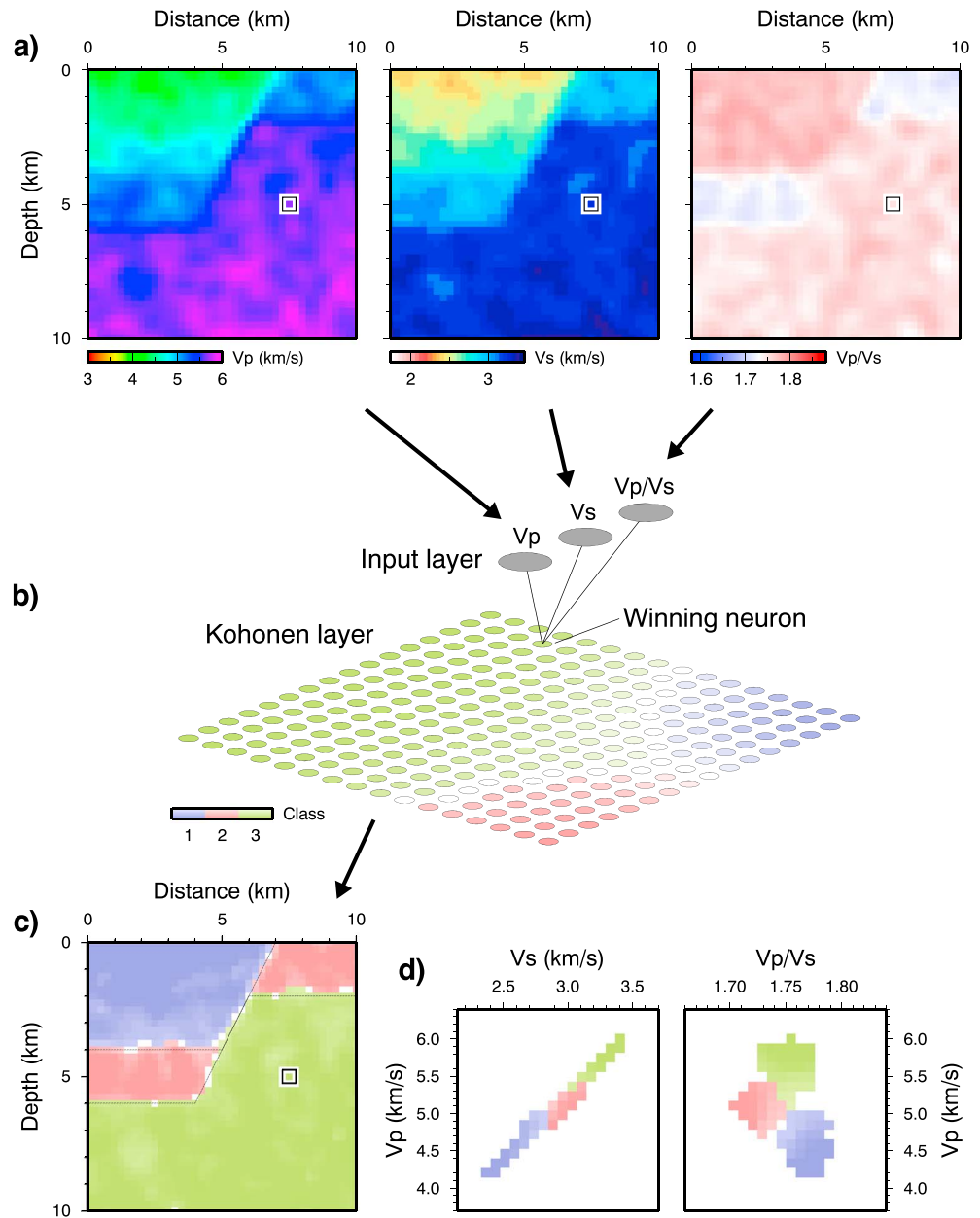


**Figure 3.** Schematic description of the SOM work flow. (a) Synthetic models were generated to demonstrate the performance of the method. (b)  $V_p$ ,  $V_s$ , and  $V_p/V_s$  values of tomographic grid cells form the input of the neural network. The winning neuron is determined based on unsupervised learning rules. After learning, color-coded regions at the Kohonen layer correspond to clusters with similar seismic properties. (c) The color-coded distribution of the classes at depth provides a lithological model. (d) The petrophysical signature of each class is shown in crossplots of  $V_p$  versus  $V_s$  and  $V_p$  versus  $V_p/V_s$ .

by random values. During the iterative learning, randomly chosen input vectors  $\vec{x}_i$  are presented to the SOM, and the winning neuron  $w$  with the weight vector  $\vec{m}_w$  most similar to the input vector is determined. A learning rule is then applied which modifies the weight vector of the winning neuron and its surrounding neurons [Kohonen, 2001]. For iteration step  $t$ , the updates of the weight vectors of all neurons  $i$  are calculated by

$$\vec{m}_i(t+1) = \vec{m}_i(t) + \lambda(t) \cdot n_{w,i}(t) \cdot (\vec{x}_i(t) - \vec{m}_i(t)). \quad (2)$$

The so-called neighborhood function  $n_{w,i}$  represents a Gaussian which is centered at the winning neuron  $w$ . Learning rate factor  $\lambda$  is used in equation (2) to control the size of the weight vector updates. The algorithm



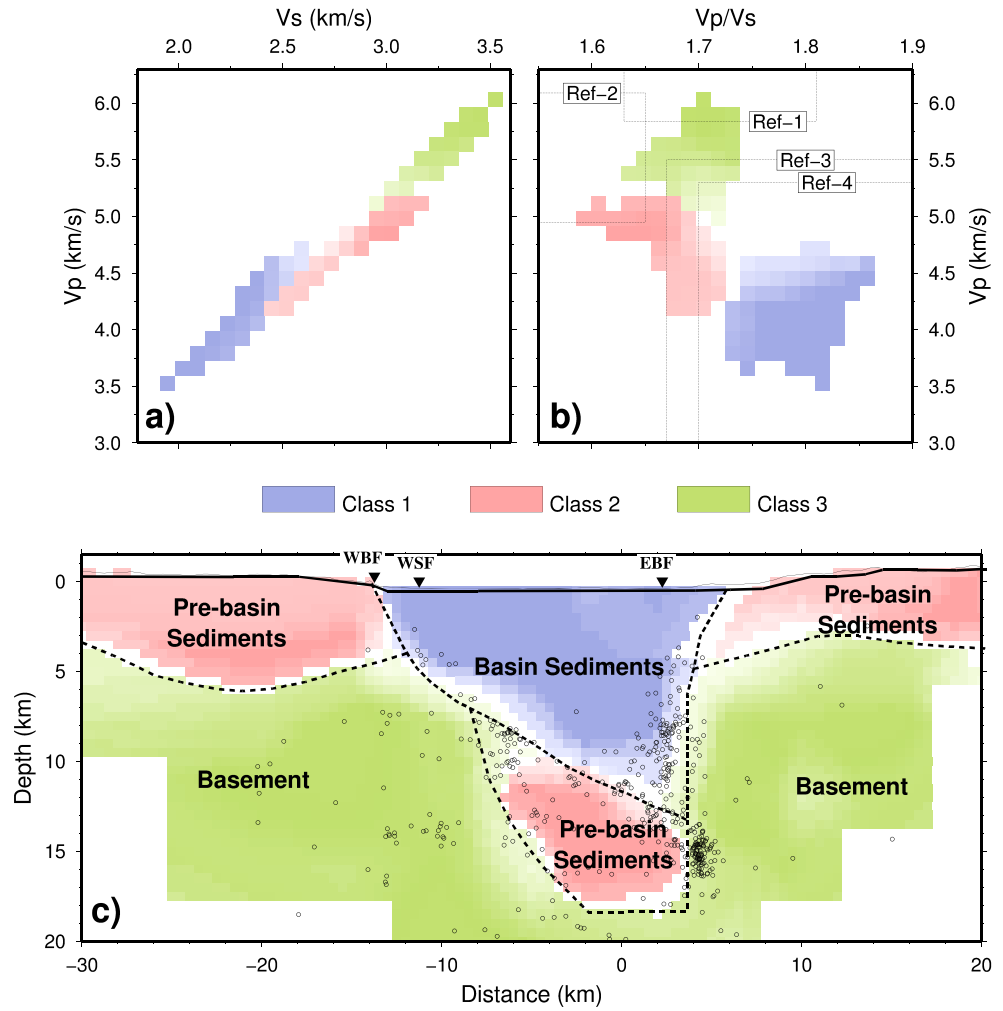


**Figure 4.** Results of the SOM analysis of the tomograms shown in Figure 2. (a) Crossplot of  $V_p$  versus  $V_s$  showing the distribution of classes 1–3. (b) Corresponding crossplot of  $V_p$  versus  $V_p/V_s$ . Ref-1: granite [Holbrook *et al.*, 1992]; Ref-2: quartzite [Holbrook *et al.*, 1992]; Ref-3: limestone [Schoen, 1996]; and Ref-4: sandstone [Schoen, 1996]. (c) Distribution of classes at depth (color-coded classes 1–3). Only regions with good resolution in  $V_p$ ,  $V_s$ , and  $V_p/V_s$  are classified. Small circles represent local earthquakes. Faults are indicated by black triangles.

converges to a behavior, which similar input vectors will be associated with neighboring regions at the Kohonen layer.

In step (3), the trained SOM is analyzed to identify regions at the Kohonen layer which show similar weight vectors at neighboring neurons in association with clustering in the seismic properties of the tomographic models. In our method [Bauer *et al.*, 2008, 2012] we determine the total gradient of the weight vectors with respect to the  $x$  and  $y$  coordinates of the Kohonen layer:

$$|\nabla \vec{m}_i| = \sqrt{\left(\frac{\partial \vec{m}_i}{\partial x}\right)^2 + \left(\frac{\partial \vec{m}_i}{\partial y}\right)^2}. \quad (3)$$

Equation (3) allows us to apply an image processing technique called watershed segmentation to define with an objective, automated scheme the extension of the different clusters at the Kohonen layer [Bauer *et al.*, 2008, 2012]. This procedure represents a main difference to other common SOM methods, where the so-called unified distance matrix (U-Matrix) is, and a manual segmentation has to be carried out based on this more noisy U-matrix function [e.g., Matos *et al.*, 2007; Tselentis *et al.*, 2007]. Each segment determined by the segmentation algorithm corresponds to a subset of input vectors with similar petrophysical properties. The

segments are color coded and labeled with classes 1–3 (Figure 3b). Strong colors indicate small total gradient values and high degree of similarity in the input data. Weak colors are related with larger total gradient values. Borders between segments are shown in white (Figure 3b).

Step (4) represents the application phase. For each tomographic grid block, the input vector is formed and the region at the segmented Kohonen layer is determined, at which the winning neuron for this input vector is located. The application to all tomographic grid blocks provides a model with the distribution of the three classes at depth. In our test, the assumed structures were successfully recovered by the SOM clustering despite of the added random variations (Figure 3c). In addition, crossplots of seismic properties are used to study the petrophysical signature of each class (Figure 3d). The latter forms the basis for the lithological interpretation of the classes.

#### 4. Results

The results are shown in Figure 4. Three classes were identified by the SOM analysis and are color coded in blue, red, and green for classes 1–3. Class 1 (blue in Figure 4) is characterized by low  $P$  velocities (3.5–4.7 km/s), low  $S$  velocities (2–2.6 km/s), and high  $V_p/V_s$  ratios (1.72–1.86). The blue area extends from the western boundary faults to the eastern boundary fault of the basin and down to depth between 5 km (west) and 12 km (east). It represents the basin sediments, i.e., the fluvial and lacustrine clastics from the Pleistocene and Holocene, the Neogene evaporites, sandstones, and conglomerates. Class 2 (red in Figure 4) is characterized by moderate  $P$  and  $S$  velocities (4–5.2 km/s and 2.5–3.2 km/s, respectively) and low to moderate  $V_p/V_s$  ratios (1.6–1.72). Class 2 was found in the upper 3–5 km east and west of the basin and is interpreted as the old prebasin sediments (Mesozoic carbonates and sediments of Permian age). A remarkable finding is that Class 2 material was also identified below the basin sediments in depths between 10 and 18 km. Class 3 (green in Figure 4) is characterized by higher  $P$  and  $S$  velocities (5.2–6.1 km/s and 3.0–3.5 km/s, respectively) and moderate  $V_p/V_s$  ratios (1.65–1.73). Tomographic grid blocks classified as Class 3 show up in the deepest parts of the model. Class 3 is interpreted as the granitic and gneissic pre-Cambrian basement as described in Förster *et al.* [2010]. To support our lithological interpretations of classes 1–3, we superimpose in Figure 4b the petrophysical signatures of granite, quartzite, limestone, and sandstone as given in the global compilations of Holbrook *et al.* [1992] and Schoen [1996], respectively.

#### 5. Discussion and Conclusions

Figure 4c shows the distribution of the classes superimposed by a simplified structural interpretation of our results. The general structure of the upper crust as derived by the SOM clustering is in agreement with former studies [e.g., Frieslander and Ben-Avraham, 1989; Garfunkel, 1997; Braeuer *et al.*, 2012b]. It shows an asymmetric basin with a vertical strike-slip fault forming the eastern boundary, and an inclined western boundary, made up of strike-slip and normal faults. At the western edge the basin sediments are reaching a depth of 5 km, directly overlying the basement. The deepest borehole in the DSB was drilled south of Mount Sedom (Figure 1) and would be located at about –10 km in our profile [Gardosh *et al.*, 1997]. Down to its total depth of 6.4 km, only basin sediments were encountered and no indications for prebasin sediment were found. In our model, at –10 km distance the basin sediments are reaching a depth of about 6 km, directly followed by the basement. Thus, we find no evidence for prebasin sediments in the western part of the DSB although a thin layer of prebasin sediments cannot be completely ruled out due to the limitations in resolution (Braeuer *et al.*, 2012b). The intersect between our profile and a N-S running seismic refraction line [Ginzburg and Ben-Avraham, 1997] is located at –5 km distance, where our model shows 8 km thick basin sediments and a 14 km deep top of the basement in agreement with Ginzburg and Ben-Avraham [1997]. At the eastern edge the basin sediments are about 13 km thick.

The presented SOM clustering indicates that the shallow layers outside of the basin show very similar petrophysical properties as the material below the eastern part of the basin fill. As the rocks at shallow depth outside of the basin are identified as prebasin sedimentary rocks [e.g., Gilboa *et al.*, 1993], we conclude that the class 2 material below the eastern part of the basin represents the buried counterpart of these prebasin sediments (Figure 4c). This interpretation is guided by the classification results from the SOM analysis which rely on the similarity in  $V_p$  and  $V_p/V_s$ . The existence of prebasin formations under the basin was predicted by

several authors [ten Brink *et al.*, 1993; Garfunkel, 1997; Ben-Avraham and Schubert, 2006; Mechie *et al.*, 2009; Choi *et al.*, 2011]. However, our results reveal for the first time a distinct body for these prebasin sedimentary rocks below the SDSB (Figure 4c). An unsolved question remains regarding the shape of this body, which apparently was not thinned in comparison with the prebasin layer east and west of the DSB. Alternatively, the body under the basin could represent a zone of mechanical softening and ductile shearing in the basement as consequence of alteration processes and presence of fluids [ten Brink *et al.*, 2006; ten Brink and Flores, 2012]. Such an interpretation would be supported by the lowered  $V_p$  values observed for class 2 material. The moderate  $V_p/V_s$  values of class 2, however, contradict such an interpretation, as the presence of fluids typically leads to increased  $V_p/V_s$  values in fractured rocks [Popp and Kern, 1994]. Hence, we favor an interpretation as prebasin sediments, despite of the unanswered question regarding the lack of thinning.

The shape of the units in our lithological model is confirmed by the superposition with the seismicity distribution [Braeuer *et al.*, 2014]. Seismic events are particularly concentrated on the eastern boundary of the basin sediments and on both the eastern and western boundaries of the prebasin sediments. We speculate that deformation as well as accumulation and release of stress are highest at lithological boundaries, where earthquakes are triggered. Noteworthy, for the alternative interpretation of the crust under the basin at 10 km–18 km depth as a ductile shear zone within the crystalline basement [ten Brink *et al.*, 2006; ten Brink and Flores, 2012] we would rather expect a widespread seismicity distribution instead of the observed pattern outlining our prebasin sedimentary body under the SDSB.

Altogether, our results indicate an asymmetric structure of the SDSB with only 5 km basin sediment thickness at the western edge and about 13 km basin sediment thickness at the eastern edge. Furthermore, we are able to image the location and dimension of the prebasin sediments, concentrated in the eastern part below the basin sediments down to 18 km depth. Our results may serve, together with other information on crustal structure and topography, as new constraints for a geodynamic modeling of the Dead Sea basin development [e.g., Petrunin and Sobolev, 2006; Deves *et al.*, 2011].

## Acknowledgments

Funding for the DESIRE project was provided by the Deutsche Forschungsgemeinschaft (DFG) and the Deutsches GeoForschungsZentrum Potsdam (GFZ). The Geophysical Institute of Israel (GII), the Natural Resources Authority (NRA) of Jordan, and the An-Najah National University in Nablus, Palestine are thanked for their support during the field work. Seismological instruments and related software were provided by the Geophysical Instrument Pool Potsdam (GIPP) of the GFZ. We are grateful to Jacek Stankiewicz, Michael Weber, and Christian Haberland for proofreading the manuscript. All the figures were created with the GMT software [Wessel *et al.*, 2013]. The manuscript benefited from helpful reviews by Amotz Agnon and Walter Mooney. The raw data used as a base for this study are accessible within the data publication of Asch *et al.* [2006].

## References

- Asch, G., A. Mohsen, B. Braeuer, R. Hofstetter, D. Jaser, R. El-Kelani, and M. Weber (2006), *DESIRE—Seismology, Dead Sea*, Deutsches GeoForschungsZentrum GFZ, Potsdam, Germany, doi:10.14470/M975513393354.
- Baço, F., V. Lobo, and M. Painho (2005), *Self-organizing Maps as Substitutes for K-Means Clustering*, *Lecture Notes Comput. Sci.*, vol. 3516, edited by V. S. Sunderam *et al.*, pp. 476–483, Springer, Berlin.
- Bauer, K., A. Schulze, T. Ryberg, S. V. Sobolev, and M. H. Weber (2003), Classification of lithology from seismic tomography: A case study from the Messum igneous complex, Namibia, *J. Geophys. Res.*, 108(B3), 2152, doi:10.1029/2001JB001073.
- Bauer, K., R. G. Pratt, C. Haberland, and M. Weber (2008), Neural network analysis of crosshole tomographic images: The seismic signature of gas hydrate bearing sediments in the Mackenzie Delta (NW Canada), *Geophys. Res. Lett.*, 35, L19306, doi:10.1029/2008GL035263.
- Bauer, K., G. Münö, and I. Moock (2012), Pattern recognition and lithological interpretation of collocated seismic and magnetotelluric models using self-organizing maps, *Geophys. J. Int.*, 189(2), 984–998, doi:10.1111/j.1365-246X.2012.05402.x.
- Ben-Avraham, Z., and G. Schubert (2006), Deep drop down basin in the southern Dead Sea, *Earth Planet. Sci. Lett.*, 251, 254–263.
- Braeuer, B., G. Asch, R. Hofstetter, C. Haberland, D. Jaser, R. El-Kelani, and M. Weber (2012a), Microseismicity distribution in the southern Dead Sea basin and its implications on the structure of the basin, *Geophys. J. Int.*, 188, 873–878, doi:10.1111/j.1365-246X.2011.05318.x.
- Braeuer, B., G. Asch, R. Hofstetter, C. Haberland, D. Jaser, R. El-Kelani, and M. Weber (2012b), High-resolution local earthquake tomography of the southern Dead Sea area, *Geophys. J. Int.*, 191, 881–897, doi:10.1111/j.1365-246X.2012.05668.x.
- Braeuer, B., G. Asch, R. Hofstetter, C. Haberland, D. Jaser, R. El-Kelani, and M. Weber (2014), Detailed seismicity analysis revealing the dynamics of the southern Dead Sea area, *J. Seismol.*, 18, 731–748.
- Choi, S., H.-J. Götze, U. Meyer, and DESIRE Group (2011), 3-D density modelling of underground structures and spatial distribution of salt diapirism in the Dead Sea Basin, *Geophys. J. Int.*, 184, 1131–1146, doi:10.1111/j.1365-246X.2011.04939.x.
- Christensen, N. I. (1996), Poisson's ratio and crustal seismology, *J. Geophys. Res.*, 101, 3139–3156.
- Deves, M., G. C. P. King, Y. Klinger, and A. Agnon (2011), Localised and distributed deformation in the lithosphere: Modelling the Dead Sea region in 3 dimensions, *Earth Planet. Sci. Lett.*, 308, 172–184.
- Eberhart-Phillips, D. (1986), Three-dimensional velocity structure in northern California Coast Ranges from inversion of local earthquake arrival times, *Bull. Seismol. Soc. Am.*, 76(4), 1025–1052.
- Evans, J. R., D. Eberhart-Phillips, and C. H. Thurber (1994), User's Manual for SIMULPS12 for Imaging  $V_p$  and  $V_p/V_s$ : A derivative of the "Thurber" tomographic inversion SIMUL3 for local earthquakes and explosions, *U.S. Geol. Surv. Open File Rep.* 94–431.
- Förster, H.-J., A. Förster, R. Oberhänsli, and D. Stromeyer (2010), Lithospheric composition and thermal structure of the Arabian Shield in Jordan, *Tectonophysics*, 481, 29–37, doi:10.1016/j.tecto.2008.11.014.
- Freund, R., Z. Garfunkel, I. Zak, M. Goldberg, T. Weissbrod, B. Derin, F. Bender, F. E. Wellings, and R. W. Girdler (1970), The shear along the Dead Sea Rift, *Philos. Trans. R. Soc. London*, 267(1181), 107–130.
- Frieslander, U., and Z. Ben-Avraham (1989), Magnetic field over the Dead Sea and vicinity, *Mar. Pet. Geol.*, 6, 148–160.
- Gardosh, M., E. Kashai, S. Salhov, H. Shulman, and E. Tannenbaum (1997), Hydrocarbon exploration in the southern Dead Sea area, in *The Dead Sea: The Lake and Its Setting*, *Oxford Monogr. on Geol. and Geophys.*, vol. 36, edited by T. M. Niemi, Z. Ben-Avraham, and J. R. Gat, pp. 57–72, Oxford Univ. Press, New York.
- Garfunkel, Z. (1981), Internal structure of the Dead Sea leaky transform (rift) in relation to plate kinematics, *Tectonophysics*, 80, 81–108.



- Garfunkel, Z. (1997), The history and formation of the Dead Sea basin, in *The Dead Sea: The Lake and Its Setting*, Oxford Monogr. on Geol. and Geophys., vol. 36, edited by T. M. Niemi, Z. Ben-Avraham, and J. R. Gat, pp. 36–56, Oxford Univ. Press, New York.
- Garfunkel, Z., and Z. Ben-Avraham (1996), The structure of the Dead Sea basin, *Tectonophysics*, 266, 155–176.
- Gilboa, Y., H. Fligelman, B. Derin, N. H. Foster, and E. A. Beaumont (1993), Zohar-Kidod-Haqanaim fields: Israel, eastern Mediterranean basin, in *Treatise of Petroleum Geology Atlas of Oil and Gas Fields*, edited by N. H. Foster and E. A. Beaumont, pp. 129–152, Am. Assoc. of Petrol. Geol., Tulsa, Okla.
- Ginzburg, A., and Z. Ben-Avraham (1997), A seismic refraction study of the north basin of the Dead Sea, Israel, *Geophys. Res. Lett.*, 24, 2063–2066, doi:10.1029/97GL01884.
- Hofstetter, R., C. Dörbath, and M. Calò (2012), Crustal structure of the Dead Sea basin from local earthquake tomography, *Geophys. J. Int.*, 189, 554–568, doi:10.1111/j.1365246X.2012.05369.x.
- Holbrook, W. S., W. D. Mooney, and N. I. Christensen (1992), The seismic velocity structure of the deep continental crust, in *Continental Lower Crust*, edited by D. M. Fountain, R. Arculus, and R. W. Kay, pp. 257–270, Elsevier, Amsterdam.
- Kashai, E. L., and P. F. Croker (1987), Structural geometry and evolution of the Dead Sea–Jordan rift system as deduced from new subsurface data, *Tectonophysics*, 141, 33–60.
- Kohonen, T. (2001), *Self-Organizing Maps*, Inf. Sci., vol. 30, 3rd ed., 501 pp., Springer, New York.
- Matos, M. C., P. L. M. Osorio, and P. R. S. Johann (2007), Unsupervised seismic facies analysis using wavelet transform and self-organizing maps, *Geophysics*, 72, 9–P21, doi:10.1190/1.2392789.
- Mechie, J., K. Abu-Ayyash, Z. Ben-Avraham, R. El-Kelani, I. Qabbani, M. Weber, and DESIRE Group (2009), Crustal structure of the southern Dead Sea basin derived from project DESIRE wide-angle seismic data, *Geophys. J. Int.*, 178, 457–478, doi:10.1111/j.1365246X.2009.04161.x.
- Muksin, U., K. Bauer, and C. Haberland (2013), Seismic  $V_p$  and  $V_p/V_s$  structure of the geothermal area around Tarutung (North Sumatra, Indonesia) derived from local earthquake tomography, *J. Volcanol. Geotherm. Res.*, 260, 27–42, doi:10.1016/j.jvolgeores.2013.04.012.
- Paasche, H., J. Troncke, K. Holliger, A. G. Green, and H. Maurer (2006), Integration of diverse physical-property models: Subsurface zonation and petrophysical parameter estimation based on fuzzy c-means cluster analysis, *Geophysics*, 71, H33–H44, doi:10.1190/1.2192927.
- Petrudin, A., and S. V. Sobolev (2006), What controls thickness of sediments and lithospheric deformation at a pull-apart basin?, *Geology*, 34, 389–392, doi:10.1130/G22158.1.
- Popp, T., and H. Kern (1994), The influence of dry and water saturated cracks on seismic velocities of crustal rocks—a comparison of experimental data with theoretical model, *Surv. Geophys.*, 15, 443–465.
- Quennel, A. M. (1958), The structural and geomorphic evolution of the Dead Sea rift, *Q. J. Geol. Soc. London*, 114, 1–24.
- Ryberg, T., J. A. Hole, G. S. Fuis, M. J. Rymer, F. Bleibinhaus, D. Stromeyer, and K. Bauer (2012), Tomographic  $V_p/V_s$  velocity structure of the California Central Coast Ranges, in the vicinity of SAFOD, from controlled-source seismic data, *Geophys. J. Int.*, 190(3), 1341–1360, doi:10.1111/j.1365-246X.2012.05585.x.
- Sagy, A., Z. Reches, and A. Agnon (2003), Hierarchic three-dimensional structure and slip partitioning in the western Dead Sea pull-apart, *Tectonics*, 22(1), 1004, doi:10.1029/2001TC001323.
- Schoen, J. H. (1996), *Physical Properties of Rocks: Fundamentals and Principles of Petrophysics*, Handbook of Geophys. Explor.: Seism. Explor., vol. 18, Pergamon, New York.
- Shamir, G. (2006), The active structure of the Dead Sea Depression, *Spec. Pap. Geol. Soc. Am.*, 401, 15–32.
- Smit, J., J.-P. Brun, S. Cloetingh, and Z. Ben-Avraham (2010), The rift-like structure and asymmetry of the Dead Sea Fault, *Earth Planet. Sci. Lett.*, 290, 74–82, doi:10.1016/j.epsl.2009.11.060.
- Stankiewicz, J., K. Bauer, and T. Ryberg (2010), Lithology classification from seismic tomography: Additional constraints from surface waves, *J. Afr. Earth Sci.*, 58, 547–552.
- ten Brink, U. S., and C. H. Flores (2012), Geometry and subsidence history of the Dead Sea basin: A case for fluid-induced mid-crustal shear zone?, *J. Geophys. Res.*, 117, B01406, doi:10.1029/2011JB008711.
- ten Brink, U. S., Z. Ben-Avraham, R. E. Bell, M. Hassounah, D. F. Coleman, G. Andreasen, G. Tibor, and B. Coakley (1993), Structure of the Dead Sea Pull-Apart Basin From Gravity Analyses, *J. Geophys. Res.*, 98(B12), 21,877–21,894.
- ten Brink, U. S., A. S. Al-Zoubi, C. H. Flores, Y. Rotstein, I. Qabbani, S. H. Harder, and G. R. Keller (2006), Seismic imaging of deep low-velocity zone beneath the Dead Sea basin and transform fault: Implications for strain localization and crustal rigidity, *Geophys. Res. Lett.*, 33, L24314, doi:10.1029/2006GL027890.
- Thurber, C. H. (1983), Earthquake locations and three-dimensional crustal structure in the Coyote Lake area, Central California, *J. Geophys. Res.*, 88(B10), 8226–8236, doi:10.1029/JB088iB10p08226.
- Thurber, C. H. (1993), Local earthquake tomography: Velocities and  $V_p/V_s$ -theory, in *Seismic Tomography: Theory and Practice*, edited by H. M. Iyer and K. Hirahara, chap. 20, pp. 563–583, Chapman and Hall, London.
- Tselentis, G.-A., A. Serpetsidaki, N. Martakis, E. Sokos, P. Paraskevopoulos, and S. Kapotas (2007), Local high-resolution passive seismic tomography and Kohonen neural networks—Application at the Rio-Antirio Strait, central Greece, *Geophysics*, 72(4), B93–B106.
- Wessel, P., W. H. F. Smith, R. Scharroo, J. F. Luis, and F. Wobbe (2013), Generic mapping tools: Improved version released, *Eos Trans. AGU*, 94, 409–410.
- Zak, I. (1967), The geology of Mt. Sedom, PhD thesis, The Hebrew Univ. of Jerusalem, 208 p.